UNIVERSIDAD DE CONCEPCIÓN
FACULTAD DE CIENCIAS FÍSICAS Y MATEMÁTICAS

Assessment of Water Quality Using Hyperspectral and Multispectral Data for the Characterization of Eutrophication in Lake Villarrica

Por: Óscar Cartes Esquivel

Tesis presentada a la Facultad de Ciencias Físicas y Matemáticas de la Universidad de Concepción para optar al grado de Magíster en Geofísica

April 2026
Concepción, Chile

Profesor Guía: Santiago Yépez
Profesor Co-Guía: Lien Rodríguez

AGRADECIMIENTOS

Agradezco el apoyo, la orientación y la constante disposición de mis profesores Santiago Yépez, Lien Rodríguez y Germán Velásquez, cuyo acompañamiento académico y motivación fueron fundamentales para el desarrollo de este trabajo. Asimismo, se reconoce el financiamiento otorgado por los proyectos FONDECYT 1221091 y 11250177 los cuales hicieron posible la realización de esta investigación.

Imprescindible fue el amor, cariño y compañía de mi madre, padre y hermano.

Hermosos y provechosos fueron los momentos de distracción y ayuda de los innumerables amigos y compañeros que hice en el camino, quienes si debiera alistarlos serían demasiados, pero cada uno dejo una marca en mi corazón.. compañeros de generación, de carrera, de facultad, del club de ajedrez y amigos de vida.

Resumen

El lago Villarrica, situado en el sur de Chile, es un recurso vital de agua dulce cuyo estado ecológico requiere una evaluación continua. El control de la calidad de sus aguas es esencial para detectar procesos de eutrofización. La clorofila-a (Chl-a) es un indicador clave de la biomasa de fitoplancton y su estimación mediante sensores satelitales permite un control eficiente y a gran escala. En este estudio se comparó el rendimiento de diferentes modelos empíricos basados en datos de reflectancia obtenidos a partir de imágenes satelitales corregidas atmosféricamente utilizando el software ACOLITE, calibrados con mediciones in-situ de Chl-a recogidas durante las estaciones de primavera y verano entre 2014 y 2024. Para cada sensor, se seleccionó la mejor combinación de bandas espectrales y se generaron modelos utilizando un procedimiento de bootstrapping con 1000 iteraciones para obtener coeficientes de regresión robustos; los modelos finales se definieron utilizando la mediana de estos coeficientes. El modelo con mejor rendimiento para Landsat-8 y 9 se basó en una combinación de bandas azul y roja (R^2= 0.79, RMSE = 2.1 µg $\cdot L^{-1}$, MAE = 1.2 µg $\cdot L^{-1}$, n = 74), mientras que para Sentinel-2, el modelo óptimo utilizó las bandas azul y verde (R^2= 0.75, RMSE = 0.8 µg $\cdot L^{-1}$, MAE = 0.72 µg $\cdot L^{-1}$, n = 112).En general, los resultados obtenidos mediante teledetección revelan un aumento gradual de los niveles de Chl-a durante la última década. Esta tendencia podría estar relacionada tanto con el calentamiento climático como con el aumento de las presiones antropogénicas, lo que refuerza la necesidad de contar con sistemas de vigilancia continua basados en observaciones satelitales. Ampliar la base de datos in-situ de Chl-a, aumentar la disponibilidad de imágenes satelitales e incorporar mediciones de reflectancia in-situ y cámaras multiespectrales es esencial para mejorar la precisión de los modelos y superar los retos que plantean la cobertura nubosa y los aerosoles.

Keywords – Landsat-8 y 9; Sentinel2-A y B; Modelos empiricos; Acolite; Clorofila-a.

Abstract

Lake Villarrica, located in southern Chile, is a vital freshwater resource whose ecological status requires continuous evaluation. Monitoring its water quality is essential for detecting eutrophication processes. Chlorophyll-a (Chl-a) is a key indicator of phytoplankton biomass and estimating it using satellite sensors enables efficient and large-scale monitoring. In this study, the performance of different empirical models based on reflectance data obtained from atmospherically corrected satellite images using ACOLITE software, calibrated with in-situ Chl-a measurements collected during the spring and summer seasons between 2014 and 2024, was compared. For each sensor, the best combination of spectral bands was selected, and models were generated using a bootstrapping procedure with 1000 iterations to obtain robust regression coefficients; the final models were defined using the median of these coefficients. The best-performing model for Landsat-8 and 9 was based on a combination of blue and red bands (R^2= 0.79, RMSE = 2.1 µg $\cdot L^{-1}$, MAE = 1.2 µg $\cdot L^{-1}$, n = 74), while for Sentinel-2, the optimal model used the blue and green bands (R^2= 0.75, RMSE = 0.8 µg $\cdot L^{-1}$, MAE = 0.72 µg $\cdot L^{-1}$, n = 112). In general, the results obtained through remote sensing reveal a gradual increase in Chl-a levels over the last decade. This trend could be associated with both climate warming and increasing anthropogenic pressures, reinforcing the need for continuous monitoring systems based on satellite observations. Expanding the in-situ Chl-a database, increasing satellite image availability, and incorporating in-situ reflectance measurements and multispectral cameras are essential to enhance model accuracy and overcome challenges posed by cloud cover and aerosols.

Keywords – Landsat-8 and 9; Sentinel-2A & B; Empirical models; ACOLITE; Chlorophyll-a.

Índice general

List of Tables

Índice de figuras

Capítulo 1

Introducción

1.1. Marco Teorico

The southern zone of Chile is abundant in water bodies, including rivers, lagoons, and lakes Fernández and Gironás (2021). Lakes are of particular interest for their high biodiversity and role as tourist attractions and natural resource sites Heino et al. (2021); Zadereev et al. (2020). Lake Villarrica, the country's third-largest by surface area after Lakes General Carrera and Llanquihue Zumelzu (2021), is among the most visited, with Pucón and Villarrica on its shores drawing large numbers of summer tourists. The watershed also supports forestry and livestock industries Ministerio del Medio Ambiente (MMA) (2020). However, tourism, industry, and urban expansion have degraded the lake's water quality, raising concerns among Chilean authorities Ministerio del Medio Ambiente (MMA) (2017). In summer, harmful algal blooms, caused by uncontrolled growth of algae and cyanobacteria, pose risks to human health and aquatic ecosystems Aguilera et al. (2023); Ladera Sur (2024); Rodríguez-López et al. (2023a); Nimptsch et al. (2016).

The trophic status of a lake, an indicator of its biological productivity relative to nutrient concentrations, is a key parameter for evaluating the effects of anthropogenic pressures. Lakes are typically classified into four categories: oligotrophic and mesotrophic, characterized by low productivity and clear waters, and eutrophic and hypertrophic, with high productivity and turbid waters Carlson (1977). Eutrophication, a natural process resulting from nitrogen and phosphorus enrichment, can shift this classification. Its rate is often accelerated by human activities, elevated spring–summer temperatures, and climate variability Campero

et al. (2024); Richardson et al. (2017).

Imaging spectrometry has become an essential tool for assessing water quality in both rivers and lakes, enabling the detection of spatial and temporal variations in key optical parameters such as chlorophyll-a (Chl-a), suspended sediments, and colored dissolved organic matter. Its high spectral resolution allows for distinguishing subtle differences in water composition, supporting the identification of pollution sources and ecosystem changes with greater precision Goyens et al. (2022); Mabit et al. (2022); Vaughn et al. (2024); Yepez et al. (2017).

Chl-a concentration, expressed in mg/m^3 or µg/L, is one of the most widely used indicators of lake productivity Cáceres-Merino et al. (2024); Talavera et al. (2024). This key pigment in plants, algae, and cyanobacteria absorbs light in the blue and red regions of the visible spectrum and reflects in the green, making its concentration a direct proxy for algal and cyanobacterial biomass. In Chile, the Dirección General de Aguas (DGA, water agency) has monitored this parameter through *in-situ* measurements since 1986 Dirección General de Aguas (DGA) (2016). Owing to its distinct optical properties, Chl-a is also estimated via remote sensing, using empirical models that relate visible and infrared reflectance to field measurements Karimi et al. (2024); Li et al. (2023); Mamun et al. (2024); Ogashawara et al. (2021); Zhao et al. (2024); Jang et al. (2024); Buma and Lee (2020).

In Chile, remote sensing has recently been incorporated into environmental quality assessments, proving effective for monitoring aquatic systems. For example, Yépez et al. (2024) developed an empirical linear model using Landsat-8 imagery to estimate Chl-a concentration in a central Chilean lake, enabling long-term monitoring of its trophic state. Similarly, studies using Sentinel-2A and 2B data Barraza-Moraga et al. (2022); Rodríguez-López et al. (2023b) have demonstrated their utility for estimating Chl-a in Chilean lakes. In the same lake, this approach has also been applied to derive Chl-a concentration and the diffuse attenuation coefficient, supporting the evaluation of water quality and its temporal dynamics Rodríguez-López et al. (2024); Ngamile et al. (2025).

The objective of this study is to evaluate the performance of various retrieval models to identify the most robust approach for estimating Chl-a concentrations in lake systems of southern Chile. The approach compares two independent empirical models: one derived from Sentinel-2A/2B (MSI sensor) imagery, and another from a combination of Landsat-8 and Landsat-9 data. Both datasets were calibrated

using atmospherically corrected surface reflectance derived from the ACOLITE processing chain, specifically designed for aquatic environments such as coastal waters, rivers, and lakes, ensuring greater accuracy in optically complex systems. Model validation was conducted by coupling in-situ Chl-a measurements with hyperspectral reflectance profiles acquired at each sampling station. This dual-model strategy offers a novel, robust, and transferable framework for water quality monitoring in diverse lacustrine environments.

Capítulo 2

Metodología

2.1. Study Area

Villarrica Lake, in the pre-Andean Araucana Region ($39°18'S$, $75°05'W$; 220 m.a.s.l), is one of Chile's largest lakes, with an area of 175 km^2, a 71 km shoreline, a volume of 21 km^3, and a maximum depth of 165 m Herrera (2021). Water temperature ranges from 9 °C in winter to 22 °C in summer (CAMELS–CR2). The Pucón River, its main tributary, supplies 90 % of inflow and nutrients, while the Toltén River is the sole outflow (Figure 1). The basin hosts about 109,016 inhabitants across Pucón, Villarrica, Curarrehue, and Cunco Ministerio del Medio Ambiente (MMA) (2020).

According to the Dirección General de Aguas (DGA), the lake is mainly oligotrophic, with seasonal mesotrophic phases Dirección General de Aguas (DGA) (2014). However, recent years have seen deterioration beyond secondary environmental quality standards for Chl-a, phosphorus, and nitrogen, largely from anthropogenic sources, leading to more frequent algal blooms Ladera Sur (2024); Dirección General de Aguas (DGA) (2018); Simón and Ceballos Sáez (2023).

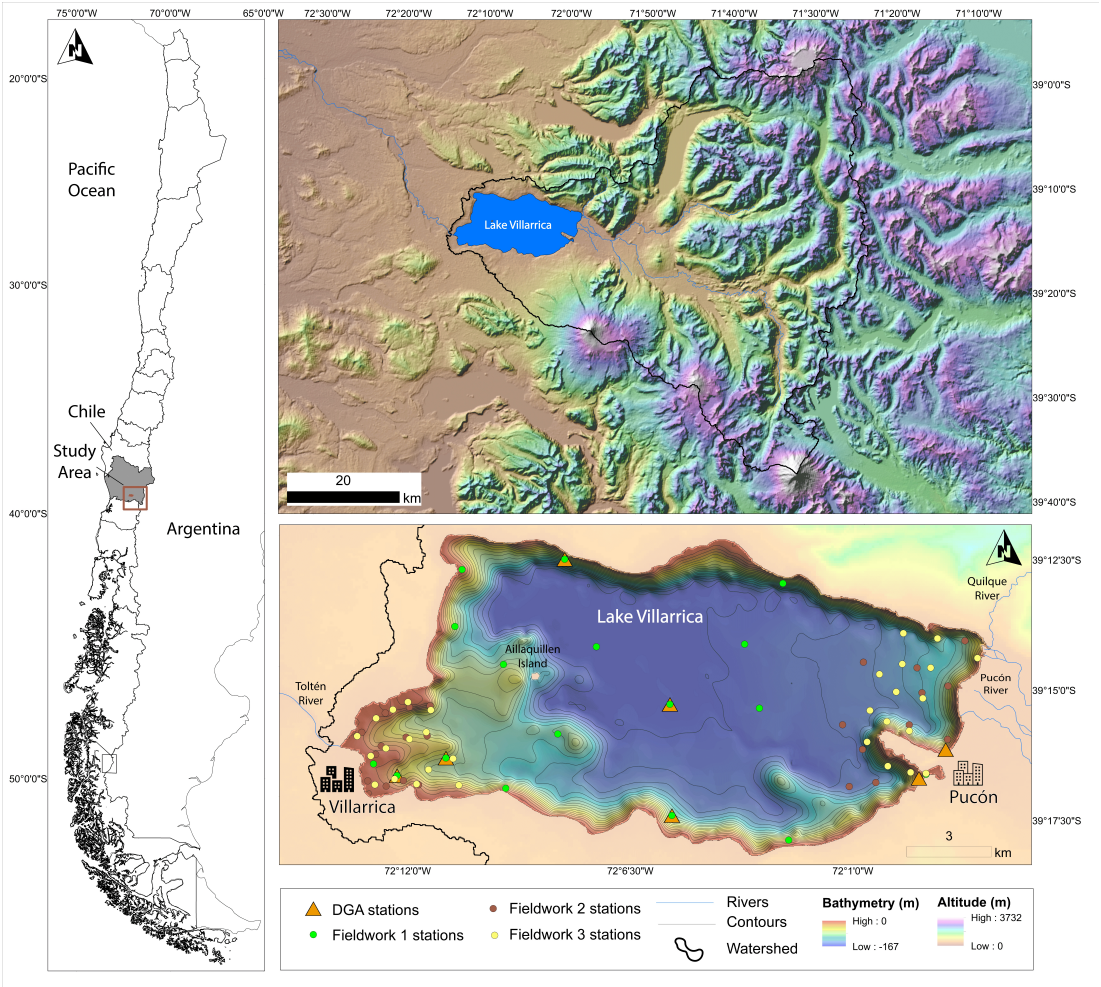

Figure 1: Geographical location and bathymetric and altitudinal features of the study area. (a) Location of Lake Villarrica in southern Chile. (b) Elevation model showing the watershed feeding the lake. (c) Bathymetric map of Lake Villarrica indicating field campaigns sampling stations (colored circles) and DGA stations (triangles). Major inflowing rivers (Toltén, Quilque, and Pucón) and Aillalquillén Island are also identified. Bathymetry is expressed in meters, with contour lines depicting relative lakebed depth.

To better understand the environmental drivers associated with these algal bloom events, the local climatological context was analyzed. Figure 2 illustrates the average climate behavior in the northern sector of Lake Villarrica, represented by mean monthly accumulated precipitation (blue bars) and mean monthly temperature (red line) for the period 2018–2025. Data were acquired from the 'Villarrica' weather station, managed by the Chilean Meteorological Directorate (available at www.agrometeorologia.cl). A marked seasonal pattern is evident, characterized by maximum precipitation during winter months (peaking in June)

and minimum values during the summer period. This dry season coincides with a progressive rise in temperature, reaching its maximum in February. This climatic regime is critically relevant to this study, as the synergy between high summer temperatures and reduced precipitation creates a scenario highly conducive to eutrophication processes and the acceleration of the algal blooms described above.

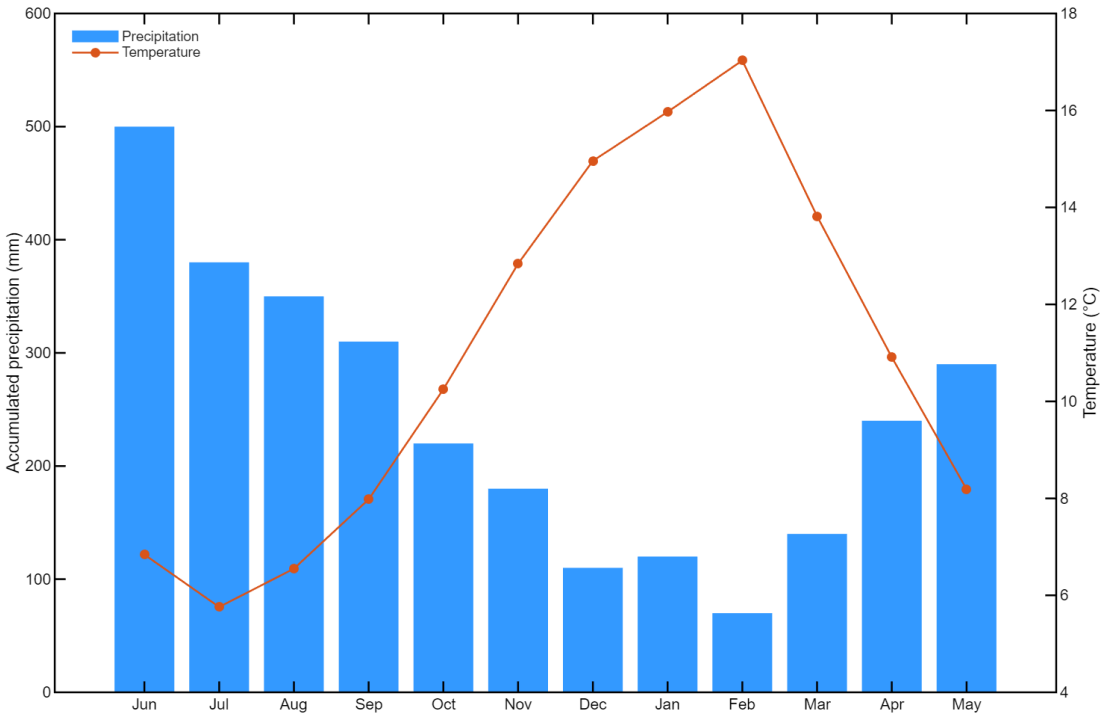

Figure 2: Monthly mean accumulated precipitation (blue bars, left axis) and monthly mean temperature (orange line, right axis) in the Villarrica lake basin, calculated for the period 2018-2024.

2.2. Data adquisition

2.2.1. Chl-a and Climatological Data

The Chl-a database was compiled from two primary sources, integrating historical and recent field measurements to provide a robust basis for assessing seasonal and interannual variations in Lake Villarrica.

While DGA records date back to 1986, this research is limited to the 2013–2023 period to guarantee matchup consistency between field data and satellite overpasses. The dataset totals 106 measurements from seven fixed stations: two near Pucón, two near Villarrica, and three in the northern, central, and southern sectors of the

lake. This design captures the spatial variability across the system. No data were available for 2018 and 2019 due to the lack of field campaigns conducted by the DGA during those years. Station names and coordinates are provided in Table A1.

Additionally, a second dataset of 75 samples was obtained through three field campaigns conducted on 10 December 2023 (21 samples), 10 March 2024 (24 samples), and 29 October 2024 (30 samples), as detailed in Table 1. Sampling was conducted between 10:00 and 15:00 h under favorable weather conditions, following a spatial grid covering the lake with higher point density near urban areas and tributary inlets to better detect potential contamination sources and spatial variability in water quality. Samples were analyzed at the EULA-Chile Environmental Science Center, Universidad de Concepción, following method 445.0 (EPA, 1997) Dirección General de Aguas (DGA) (2017).

Climatological data were obtained from the online platform of the "Instituto de Investigaciones Agropecuarias de Chile" (INIA) Instituto de Investigaciones Agropecuarias (INIA) (2025), which operates a national network of automatic weather stations. Records from the "San Enrique, Pucón" station (39.26° S, 71.86° W; 279 m a.s.l.), located on the eastern shore of Lake Villarrica, were used. This station provides continuous meteorological measurements; in this study, emphasis was placed on the temporal variability of air temperature to assess its potential relationship with Chl-a concentrations and algal bloom events in the lake.

Table 1: Descriptive statistics of Chl-a concentrations (µg $\cdot L^{-1}$) measured during the field campaigns conducted as part of the Fondecyt Project 1221091.

Monitoring Campaign	Date	N° Data	Mean	Std	Max	Min
1	December 9, 2023	24	0.6	0.4	1.5	0.1
2	March 10, 2024	24	0.4	0.1	0.6	0.2
3	October 30, 2024	30	5.0	2.2	10.2	0.9

2.2.2. Satellite data

Satellite imagery from Landsat-8, Landsat-9, and Sentinel-2A/2B were acquired for each sampling date to calculate water surface reflectance, given the established relationship between spectral response and Chl-a concentration due to light interactions at specific wavelengths Cillero Castro et al. (2020). Image selection prioritized acquisitions closest to sampling dates, ensuring minimal aerosol and

atmospheric distortion. Although a total of 71 images comprising 22 from Landsat-8, 3 from Landsat-9, 25 from Sentinel-2A, and 21 from Sentinel-2B were initially processed, a subset was subsequently discarded due to significant temporal gaps between acquisition and sampling or unfavorable atmospheric conditions European Space Agency (ESA) (2025); United States Geological Survey (USGS) (2025). The final number of valid images used for each satellite and sensor group is summarized in Table B1, while detailed specifications for the selected datasets are provided in Tables B2 and B3.

Landsat-8 (2013) and Landsat-9 (2021), together with ESA's Sentinel-2A (2015) and Sentinel-2B (2017), provide essential spectral and spatial capabilities for aquatic ecosystem monitoring Xu et al. (2024). Landsat-8/9 deliver 30 m resolution in most visible and near-infrared bands, with a 16 day revisit per satellite, ensuring regular coverage of Lake Villarrica during key seasonal periods Dokulil (2014). Sentinel-2A/B offers up to 10 m spatial resolution in the visible and infrared bands and a combined five day revisit, enabling more frequent acquisitions near field sampling dates Pahlevan et al. (2021). Thus, combining Landsat-8/9 and Sentinel-2A/B imagery provided broad temporal coverage and spatial detail, enabling comparison and validation of in-situ measurements with satellite data, and supporting comprehensive temporal–spatial analyses of water quality in Lake Villarrica Nguyen et al. (2024).

2.2.3. Spectral Signature for Surface Water Analysis

A FieldSpec® 4 spectroradiometer (Analytical Spectral Devices Inc.), covering 350–2500 nm with 3 nm spectral resolution, was used to acquire surface water spectral signatures in Lake Villarrica. Measurements were taken on 29 October 2024 during the third monitoring campaign, concurrently with Chl-a sampling, yielding 15 spectral profiles from sites in front of Pucón's urban area and near tributary inlets. The campaign was conducted under stable atmospheric conditions, with clear skies, with minimal wave action. These conditions ensured high-quality surface reflectance measurements by minimizing sunglint and atmospheric scattering. This instrument has been previously applied by Yépez et al. (2024) in Laguna Grande de San Pedro de la Paz Yépez et al. (2024), and the acquisition and processing of spectral data followed the guidelines of Milton and Mobley Milton (1987); Mobley (1999). Only six signatures were selected from the remaining set to represent the

Chl-a gradient; this focused selection serves to validate the satellite models against high-fidelity in-situ hyperspectral data (Figure 4).

To estimate the above-water remote sensing reflectance (R_{rs}), the ratio between the water-leaving radiance ($L_w(\lambda)$)) and the downwelling irradiance ($Ed(\lambda)$) was calculated, as expressed in Equation 1:

$$R_{rs}(\lambda) = \frac{L_w(\lambda)}{E_d(\lambda)} \quad (\mathrm{sr}^{-1}) \tag{2.2.1}$$

The value of $Ed(\lambda)$) was derived using a calibrated white reference panel (Spectralon®, Labsphere Inc.) that acts as a Lambertian surface, allowing for the approximation of the spectral irradiance incident on the water surface.

To reduce high frequency noise without eliminating relevant spectral features such as peaks and slopes associated with photosynthetic pigments and suspended matter a Savitzky–Golay smoothing filter was applied. This method preserves the shape of spectral bands and their derivatives, facilitating the extraction of spectral indices and subsequent correlation with Chl-a concentration. In this study, a window of 21 samples and a second-order polynomial were used, parameters that have been shown to achieve an adequate balance between smoothing and preservation of spectral detail in hyperspectral water quality studies Lin et al. (2024); Wang et al. (2024b); Xing et al. (2024).

Finally, to ensure spectral consistency between in-situ and satellite observations, field reflectance measurements acquired with the ASD FieldSpec-4 were convolved with the spectral response functions (SRF) of Landsat-8/9 OLI and Sentinel-2 MSI sensors. This step allowed the simulation of sensor specific bands from hyperspectral data, reducing spectral mismatch and improving the physical comparability between platforms. The SRFs were obtained from the official Landsat OLI documentation and Sentinel-2 supplemental datasets European Space Agency (2023); U.S. Geological Survey (2021). This approach minimizes uncertainties associated with differences in band width, central wavelength, and sensor calibration, and provides a robust framework for evaluating spectral indices across multiple satellite systems.

2.2.4. ACOLITE: Atmospheric correction

For Chl-a detection in Lake Villarrica, satellite images from Landsat-8/9 and Sentinel-2A/B were atmospherically corrected using ACOLITE (Atmospheric

Correction for OLI "Lite"), a tool developed by the Royal Belgian Institute for Natural Sciences (RBINS) for coastal and inland waters German et al. (2024); Sivakumar et al. (2024). Atmospheric effects, attenuation of water-leaving radiance and additional path radiance from scattering by particles, gases, and aerosols, were minimized to recover true surface reflectance from top-of-atmosphere radiance Allam and Allam (2024); Wang et al. (2024a). ACOLITE applies the libRadtran radiative transfer model with ERA5 profiles for molecular and gas corrections, and the Dark Spectrum Fitting (DSF) algorithm for aerosol removal Vanhellemont and Ruddick (2021, 2018); Vanhellemont et al. (2024), enabling accurate retrieval of visible and near-infrared reflectance for water quality analysis

2.3. Development and validation of models

2.3.1. Selection of spectral indices

To estimate Chl-a concentration in Lake Villarrica, several spectral indices and band combinations were evaluated using four satellite data configurations: a unified Land-sat-8/9 dataset and three Sentinel-2 datasets (Sentinel-2A, Sentinel-2B, and their combined observations). The separation of Sentinel-2A and 2B datasets was designed to assess potential radiometric and spectral differences between sensors, which may influence the consistency of Chl-a retrievals. In particular, variations in signal-to-noise ratio, calibration, and spectral response functions could affect the sensitivity of red and red-edge bands to phytoplankton dynamics. The combined Sentinel-2 dataset was also analysed to determine whether increased temporal density improves the robustness of empirical relationships. The configuration showing the highest predictive performance and stability was selected for subsequent model calibration and validation.

Reflectance values were extracted by delineating buffers, or regions of interest (ROIs), centered on the field measurement sites. Buffer was set to 30 m for Sentinel-2 and 60 m for Landsat-8 and 9, corresponding to their spatial resolutions of 10 m and 30 m, respectively. This methodology ensures that the extracted reflectance reflects an average of the surrounding pixels rather than a single point, thereby reducing signal noise and mitigating potential georeferencing discrepancies between the satellite imagery and in-situ measurements. For each buffer, the reflectance was calculated as the average of all pixels falling within the area.

Using these values, different spectral indices, individual spectral bands, and three-band combinations commonly reported in the literature were computed, as summarized in Table 2. The following inter-band combinations were additionally evaluated using Eqs. (2–4):

$$\text{Ratio Index} = \frac{b_i}{b_j} \tag{2.3.1}$$

$$\text{Normalized Difference Index} = \frac{(b_j - b_i)}{(b_j + b_i)} \tag{2.3.2}$$

$$\text{Sum Index} = b_i + b_j \tag{2.3.3}$$

In these expressions, b_i and b_j represent the i-th and j-th spectral bands, respectively. For the Sentinel-2A MSI sensor, we considered the bands from the aerosol to the near-infrared region, totaling nine spectral bands. In the case of the Landsat-8 and 9 OLI sensors, the same spectral range was used, but with the addition of two ACOLITE derived bands located between the green and red regions, resulting in seven spectral bands.

Table 2: Spectral indices and band combinations.

Spectral Index	Equation	References
Normalized Difference Turbidity Index (NDTI)	$NDTI = \frac{RED - GREEN}{RED + GREEN}$	Mansourmoghaddam et al. (2022)
Normalized Difference Vegetation Index (NDVI)	$NDVI = \frac{NIR - RED}{NIR + RED}$	Han and Niu (2020)
Normalized Difference Chlorophyll Index (NDCI)	$NDCI = \frac{RedEdge1 - RED}{RedEdge1 + RED}$	Mishra and Mishra (2012)
Superficial Algae Bloom Index (SABI)	$SABI = \frac{NIR - RED}{BLUE + GREEN}$	Pan et al. (2024)
Green Normalized Difference Vegetation Index (GNDVI)	$GNDVI = \frac{NIR - GREEN}{NIR + GREEN}$	Mansourmoghaddam et al. (2022)
Normalized Difference Red Edge (NDRE)	$NDRE = \frac{NIR - RedEdge2}{NIR + RedEdge2}$	Niu et al. (2024)
Water Body Chlorophyll Index (WBCI)	$WBCI = \frac{RED}{RedEdge1}$	Barraza-Moraga et al. (2022)
Green Chlorophyll Index (GCI)	$GCI = \frac{NIR}{GREEN} - 1$	Rodríguez-López et al. (2024)
MERIS Terrestrial Chlorophyll Index (MTCI)	$MTCI = \frac{RedEdge1 - RED}{RedEdge3 - RED}$	Frampton et al. (2013)
Red Edge Chlorophyll Index (RECI)	$RECI = \frac{NIR}{RedEdge1} - 1$	Muramatsu (2019)
Turbidity Index (TI)	$TI = \frac{RED}{GREEN}$	Gholizadeh et al. (2016)

Once in-situ Chl-a values and spectral combinations from Landsat-8/9 and Sentinel-2 were available, empirical relationships were established between both variables. Spectral indices reported in the literature (Table 2) and additional band combinations (Eqs. 2–4) were first evaluated using the coefficient of determination (R^2). The best-performing indices were subsequently fitted using linear, exponential, and logarithmic models to determine the model that provided the highest goodness of fit.

2.3.2. Optimization and validation of empirical models

Once the spectral band combinations exhibiting the strongest correlation with Chl-a concentration were determined for each sensor, the dataset was divided into 80 % for model training and 20 % for validation. This partition ensured that model performance was assessed using unseen data while maintaining an adequate number of observations for model training.

To account for sampling variability and reduce the influence of potential outliers, a bootstrapping procedure with 1000 iterations was applied to the calibration

subset. For each iteration, regression coefficients were estimated from resampled datasets, generating empirical distributions of the model parameters. The median coefficients were then used to construct the final empirical models for Sentinel-2 and Landsat-8/9. This approach improves the robustness and stability of parameter estimation, particularly when working with moderate sample sizes and heterogeneous environmental conditions.

The independent validation dataset consisted of 14 samples for Landsat and 22 samples for Sentinel-2, while the remaining 60 and 90 samples were used for model calibration. Model performance was evaluated using statistical metrics including the coefficient of determination (R^2), Root Mean Square Error (RMSE), Mean Absolute Error (MAE), and Mean Absolute Percentage Error (MAPE), following established practices in environmental modelling and time series forecasting Dagnino S. (2014); Hyndman and Athanasopoulos (2018).These indicators provide complementary information on model accuracy, bias, and relative predictive performance across a range of Chl-a concentrations. The following equations (5–7) describe each statistical indicator.

- **Coefficient of determination (R^2)**

$$R^2 = 1 - \frac{\sum_{i=1}^{n}(y_i - \hat{y}_i)^2}{\sum_{i=1}^{n}(y_i - \bar{y})^2} \tag{2.3.4}$$

- **Mean square error (RMSE)**

$$RMSE = \sqrt{\frac{1}{n}\sum_{i=1}^{n}(y_i - \hat{y}_i)^2} \tag{2.3.5}$$

- **Mean absolute error (MAE)**

$$MAE = \frac{1}{n}\sum_{i=1}^{n}|y_i - \hat{y}_i| \tag{2.3.6}$$

Capítulo 3

Resultado

The results section is structured to first describe the statistical characteristics and distribution of in-situ Chl-a measurements, followed by the analysis of field spectroscopy data. Next, the selection and evaluation of the most suitable spectral indices are presented, forming the basis for the development of predictive models using Landsat-8/9 and Sentinel-2A imagery. Finally, spatial distribution maps are generated to illustrate the variability and patterns of Chl-a concentrations across Lake Villarrica.

3.1. in-situ data on Chl-a concentration

Figure 3 summarizes the statistical distribution of Chl-a concentrations derived from the historical monitoring program conducted by the Dirección General de Aguas (DGA) since 2013, together with measurements collected during the 2023 and 2024 field campaigns.

Panel A shows the frequency histogram, indicating that more than 60 % of the observations are below 2 µg·L^{-1} and over 80 % remain under 5 µg·L^{-1}. The dataset exhibits a pronounced right-skewed distribution, characterized by low baseline concentrations and sporadic high-magnitude events, with values exceeding 10 µg·L^{-1} and peak concentrations surpassing 20 µg·L^{-1}. Panel B presents boxplots for the main monitoring stations. Median Chl-a concentrations at all sites remain below the mesotrophic threshold (5–10 µg·L^{-1}), indicating generally low phytoplankton biomass. However, several outliers exceed this range, particularly at La Poza, the Villarrica shoreline, and the central basin, where concentrations

above 15 µg·L^{-1} were occasionally recorded. These results suggest that Lake Villarrica predominantly exhibits oligotrophic to mesotrophic conditions Carlson (1977); Dirección General de Aguas (DGA) (2014), but is subject to localized and episodic increases in phytoplankton biomass. Such events are consistent with reported algal bloom occurrences and highlight the spatial and temporal variability of trophic status within the lake. This variability underscores the importance of high-resolution and temporally consistent remote sensing approaches to capture short-term bloom dynamics and improve monitoring of eutrophication processes in Lake Villarrica.

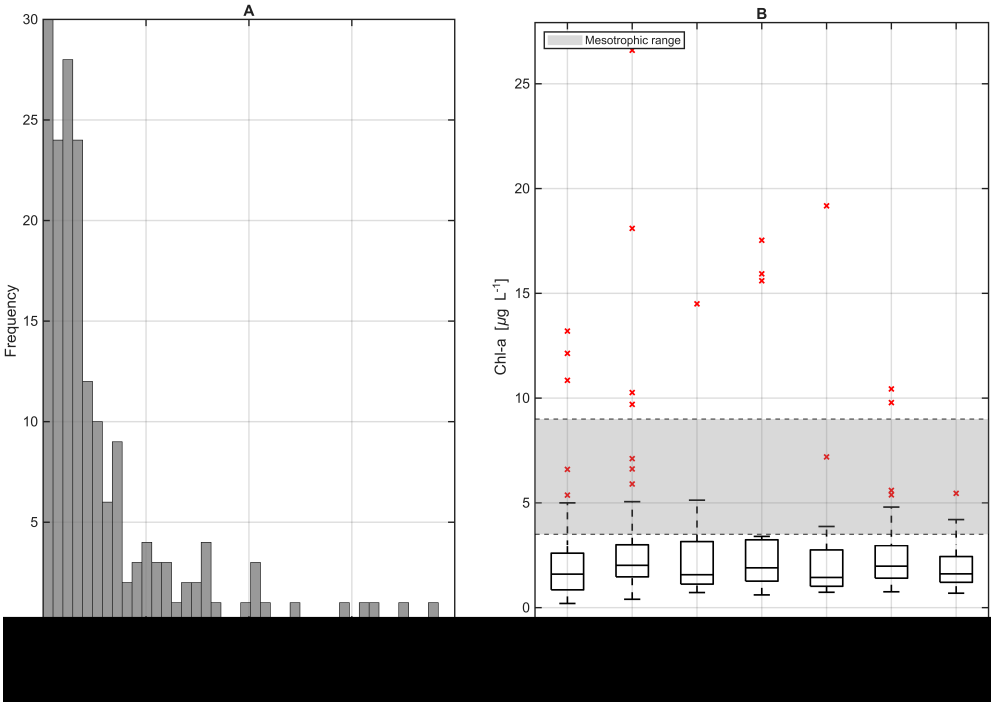

Figure 3: Histogram of Chl-a concentrations. (A) combining DGA and field campaign data, and boxplots for DGA monitoring stations (B), both based on observations from 1986 to 2024.

3.2. Models for Landsat-8 and 9 and Sentinel-2A and B

3.2.1. Hyperspectral data

Field spectroscopy measurements acquired using the ASD FieldSpec-4 radiometer were used to characterize the optical response of surface waters in Lake Villarrica

and to support the selection of relevant spectral features for satellite-based Chl-a retrieval. Figure 4 presents six representative spectral signatures collected in the northeastern tributary sector, an area of particular interest due to the influence of river inflows that can modify nutrient supply, optical properties, and local phytoplankton dynamics. Each spectrum was paired with a simultaneous in-situ Chl-a measurement, with concentrations indicated in the legend and represented by a color gradient.

Reflectance spectra were derived following standard radiometric procedures, including reference panel calibration and correction for acquisition geometry. Several spectra were discarded due to sun-glint contamination and unstable illumination conditions. The retained spectra showed a consistent relationship between reflectance and Chl-a concentration and were therefore used for further analysis. Although the number of paired observations was limited, this dataset was intended primarily to identify spectrally sensitive regions and to support the design of satellite-based empirical models rather than to establish final calibration relationships. The spectral signatures cover the visible to near-infrared range (350–1000 nm), capturing key wavelengths relevant for phytoplankton detection. Strong absorption features are observed in the blue region (440 nm), followed by increasing reflectance in the green transition zone (500–580 nm). This behavior is consistent with the spectral properties of Chl-a, which absorbs efficiently in the blue and red regions while showing enhanced reflectance in the green domain. A pronounced absorption feature is observed around 670 nm, corresponding to the red absorption maximum of Chl-a. Beyond 700 nm, reflectance decreases sharply in the near-infrared due to strong absorption by pure water, limiting sensitivity in this spectral region. The observed spectral patterns also reflect the oligotrophic to mesotrophic conditions of Lake Villarrica, where relatively low pigment concentrations and high-water transparency enhance the contrast between absorption and scattering processes. In addition, tributary inflows may contribute dissolved organic matter and suspended particles, which can influence the spectral response, particularly in the blue region.

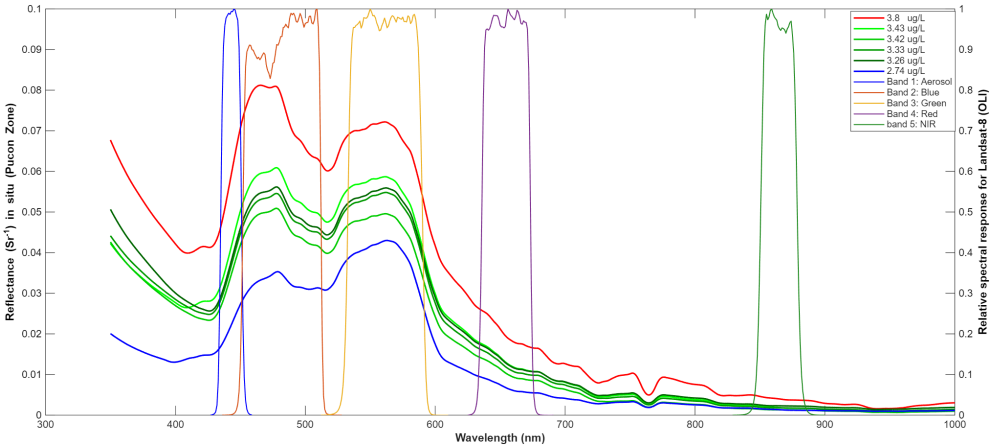

Figure 4: Surface water spectral signatures from Lake Villarrica measured with a field spectroradiometer, along with Chl-a concentrations. Landsat-8 OLI band response curves are overlaid for comparison.

Table 3 summarizes the coefficients of determination between Chl-a concentration and band-integrated reflectance values computed according to the spectral response functions of Landsat-8/9 and Sentinel-2A/B. The highest correlations were observed in the blue ($R^2 = 0.88$) and red ($R^2 = 0.82$) regions for both constellations, consistent with the well established absorption features of Chl-a. The green band also exhibited strong correlations ($R^2 = 0.80$), highlighting its importance in band-ratio algorithms. Sentinel-2A/B additionally showed moderate correlations in the red-edge region ($R^2 = 0.57$–0.78), reflecting the sensitivity of these wavelengths to phytoplankton biomass and physiological status. In contrast, Landsat-8/9 lacks red-edge bands, which limits its sensitivity in this transition domain. Near-infrared bands exhibited weaker relation ships ($R^2 = 0.51$), likely due to strong water absorption and reduced signal-to-noise under low Chl-a conditions.

Table 3: Coefficient of determination (R^2) between Chl-a concentrations and in-situ spectral signatures. The wavelengths correspond to the integrated values according to the spectral response of each band for Landsat-8/9 and Sentinel-2A/B satellites.

Satellite	Blue	Green	Red	Red edge 1	Red edge 2	Red edge 3	NIR	NIR 2
Landsat-8 and 9	0.88	0.80	0.82	–	–	–	0.51	–
Sentinel-2A	0.88	0.80	0.82	0.78	0.59	0.57	0.54	0.51

These results are further supported by Figure 5, which shows the spectral variation of the coefficient of determination across the full ASD wavelength range. The highest R^2 values, consistently above 0.8, occur in the visible region (400–700

nm), confirming that this spectral domain provides the strongest sensitivity to Chl-a variability. In contrast, R^2 values decline sharply beyond 720 nm, where water absorption dominates. This pattern highlights the central role of visible wavelengths for algorithm development and provides a robust basis for selecting optimal spectral indices for estimating Chl-a concentrations in Lake Villarrica.

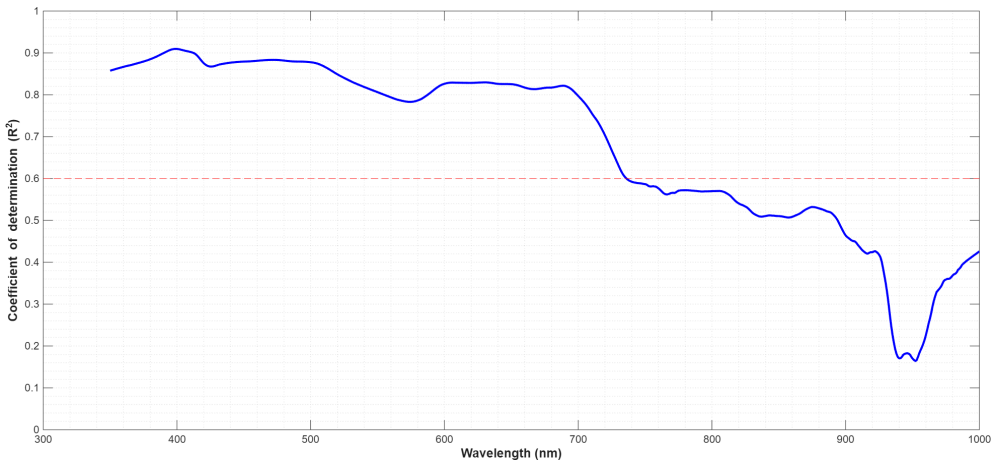

Figure 5: Coefficient of determination (R^2) between Chl-a concentration and in-situ spectral reflectance measured with a field spectroradiometer across the 300–1000 nm range.

3.2.2. Spectral band selection and model development

The relationship between in-situ Chl-a concentrations and different spectral band configurations was evaluated using the coefficient of determination (R^2). As shown in Figure 6, the analysis included individual spectral bands, as well as band combinations derived from Equations (3), (4), and (5), in addition to widely used indices summarized in Table 2. This approach aimed to identify robust spectral predictors across sensors while accounting for differences in spectral response functions and radiometric sensitivity.

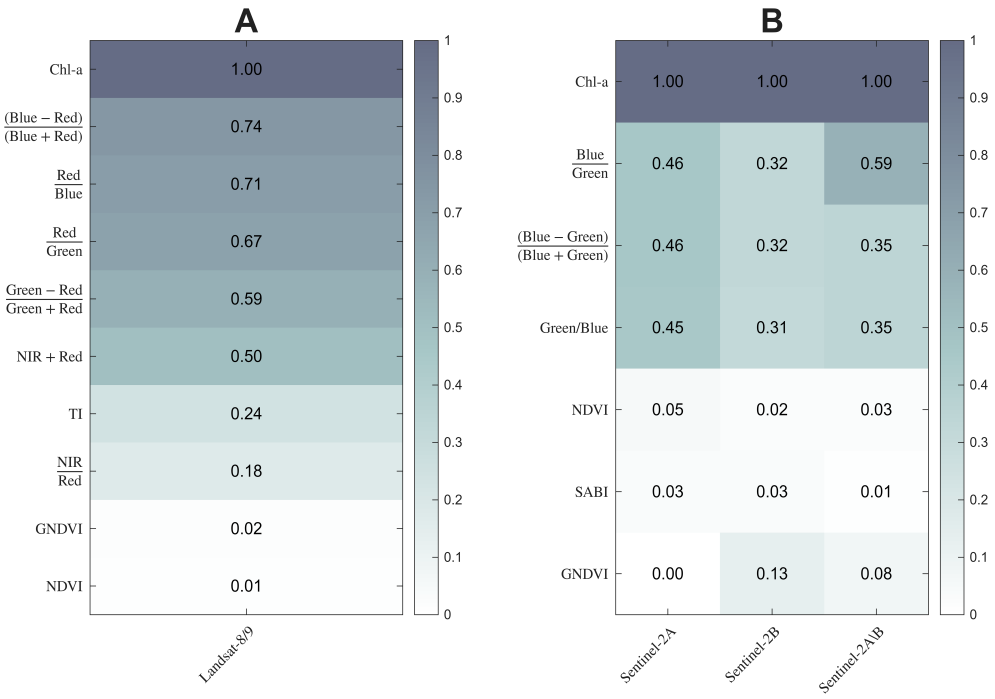

Figure 6: Coefficient of determination (R^2) obtained from a preliminary exploratory analysis assessing the linear correlation between Chl-a concentrations and surface reflectance from Landsat 8/9 and Sentinel-2 imagery.

Sentinel-2B and the combined Sentinel-2A and 2B datasets were excluded from further modelling because their correlations were systematically lower. This difference is likely related to variations in acquisition dates, atmospheric correction uncertainty, and differences in the distribution of Chl-a concentrations rather than intrinsic sensor limitations.

Using the selected spectral configurations, exponential models were calibrated for Landsat-8/9 and Sentinel-2A. Model robustness was assessed through bootstrap resampling, which allowed estimation of parameter uncertainty and improved predictive stability. This procedure increased the coefficients of determination to $R^2 = 0.79$ for Landsat-8/9 and $R^2 = 0.75$ for Sentinel-2A. The statistical performance metrics are summarized in Table 4, while a comparison between exponential and linear formulations is provided in Table C1 of Appendix C.

Prediction errors were lower for Sentinel-2A (RMSE = 0.88 µg·L^{-1}; MAE = 0.72 µg·L^{-1}) than for Landsat-8/9 (RMSE = 2.18 µg·L^{-1}; MAE = 1.2 µg·L^{-1}), indicating improved performance. This difference reflects the broader concentration range covered by the Landsat dataset, which included values up to 20 µg·L^{-1}, whereas Sentinel-2A observations were limited to approximately 5

µg·L^{-1}. Consequently, higher prediction errors for Landsat are expected due to the increased variability and non-linear optical response at elevated phytoplankton concentrations.

Table 4: Information and statistics from Landsat-8 and 9 and Sentinel-2A models.

Satellite	**Model Predictor**	**Equation**	$\mathbf{N_{train}}$	$\mathbf{N_{test}}$	$\mathbf{R^2}$	**RMSE** (µg $\mathbf{L^{-1}}$)	**MAE** (µg $\mathbf{L^{-1}}$)
Landsat-8/9	$\frac{\text{Blue} - \text{Red}}{\text{Blue} + \text{Red}}$	$56{,}8\, e^{-7{,}4x}$	60	14	0.79	2.1	1.2
Sentinel-2A	$\frac{\text{Green}}{\text{Blue}}$	$0{,}06\, e^{-3{,}05x}$	90	22	0.75	0.88	0.72

Figures 7 and 8 illustrate the best-performing models for Landsat-8/9 and Sentinel-2A, respectively. For Landsat-8/9, the exponential model captures the general decrease in Chl-a with increasing normalized difference index values. However, residual analysis indicates increasing uncertainty at concentrations above 10 µg·L^{-1}, suggesting potential saturation effects and reduced sensitivity under higher biomass conditions. In contrast, the Sentinel-2A model exhibits more stable residuals and reduced systematic bias, particularly within the low to moderate concentration range.

For Sentinel-2A (Figure 8), panel (a) illustrates the exponential model developed using the Green-Blue ratio index, where the fitted line (red) aligns closely with the distribution of observed data points. Panel (b) shows a high correlation (R^2 = 0.75), the residuals are more evenly distributed, indicating greater model stability and fewer systematic errors compared with Landsat-8/9. Although the Sentinel-2A based model exhibits a slightly lower correlation coefficient, it is supported by a larger dataset and demonstrates improved accuracy in predicting low to moderate Chl-a concentrations.

Overall, the results highlight that visible spectral combinations provide the most robust predictors for Chl-a retrieval in Lake Villarrica. While Landsat-8/9 offers a longer historical record and captures a wider concentration range, Sentinel-2A demonstrates improved sensitivity for detecting low phytoplankton biomass due to its higher spatial and spectral resolution. These findings support the complementary use of both sensors for long-term monitoring and near-real-time water quality assessment.

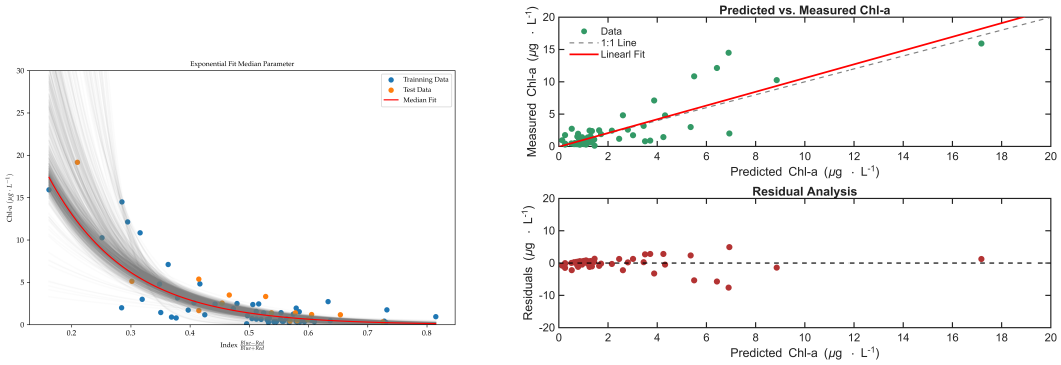

(a) **(b)**

Figure 7: Panel (a) shows a scatter plot illustrating the relationship between Chl-a data and the combination of bands (blue - red) / (blue + red) from Landsat-8 and 9 satellites (red line) together with the test data and data used to train the model. Panel (b) above shows the predicted values vs. the measured values together with the fitted line (red line) and another straight line with a slope of 1. Panel (b) below shows the model residuals calculated as the predicted data minus the measured data.

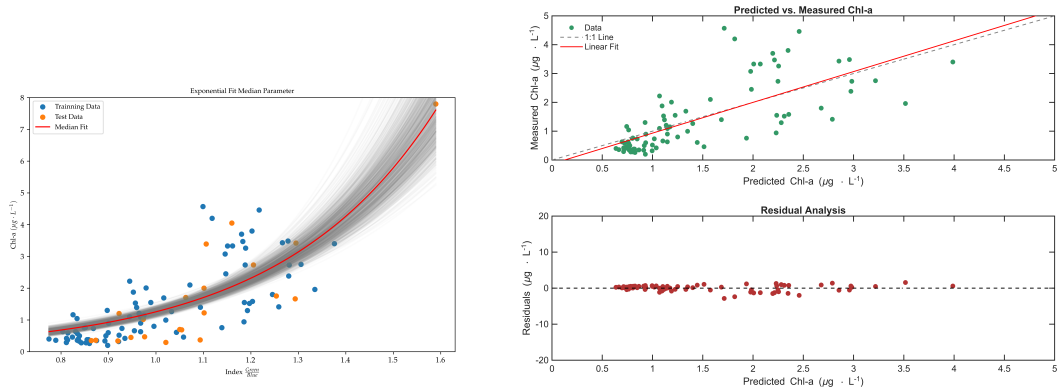

(a) **(b)**

Figure 8: Panel (a) shows a scatter plot illustrating the relationship between Chl-a data and the combination of bands Green/ Blue from Sentinel-2A (red line) together with the test data and data used to train the model. Panel (b) above shows the predicted values vs. the measured values together with the fitted line (red line) and another straight line with a slope of 1. Panel (b) below shows the model residuals calculated as the predicted data minus the measured data.

3.2.3. Spatial Distribution of Chl-a

To assess the spatial variability of Chl-a in Lake Villarrica, the retrieval models developed for Landsat-8/9 and Sentinel-2A were applied to atmospherically corrected satellite imagery. This approach converted pixel-level reflectance, through the selected spectral indices, into Chl-a concentrations, enabling the generation of spatial distribution maps that provide a synoptic view of phytoplankton biomass across the lake. These maps represent a key outcome of this study, as they reveal spatial heterogeneity, seasonal variability, and areas prone to phytoplankton accumulation and bloom formation.

Figures 9 and 10 present Landsat-8/9 derived Chl-a maps for summer and spring seasons covering 2013–2015 and 2022–2024. During the earlier period (2013–2015), the lake was predominantly characterized by low Chl-a concentrations, with most pixels below 2 µg·L^{-1}, consistent with oligotrophic conditions. In contrast, the more recent period (2022–2024) shows a progressive increase in Chl-a, particularly during spring, with concentrations reaching 3–4 µg·L^{-1} in several nearshore sectors. A distinct algal bloom is observed in the eastern region of the lake during the summer of 2022 (Figure 9D). Although some scenes present partial spatial coverage, the temporal comparison suggests increasing phytoplankton biomass in recent years. This pattern is especially evident in nearshore areas influenced by tributary inputs and urban pressures (e.g., Pucón).

Figures 11 and 12 present Sentinel-2A derived Chl-a maps for summer and spring between 2017–2019 and 2022–2024. The higher spatial resolution of Sentinel-2A reveals fine scale spatial variability and nearshore gradients not fully captured by Landsat. Similar to the Landsat results, early years (2017–2019) show consistently low Chl-a concentrations, whereas recent years display higher values and increased spatial heterogeneity. A bloom event in the eastern sector during summer 2022 is clearly resolved (Figure 11D). During spring, elevated Chl-a levels are more frequently observed in shallow and littoral zones, while the central pelagic region remains relatively stable and low.

The observed spatial patterns indicate that Lake Villarrica remains predominantly oligotrophic but exhibits increasing frequency of localized and episodic mesotrophic conditions. The concentration of higher Chl-a values in nearshore and tributary-influenced sectors suggests that external nutrient inputs and hydrological connectivity play a key role in phytoplankton dynamics. These findings highlight

the importance of continuous satellite monitoring for early detection of bloom-prone areas and support the use of multisensor approaches combining Landsat and Sentinel data for long-term and high-resolution water quality assessment.

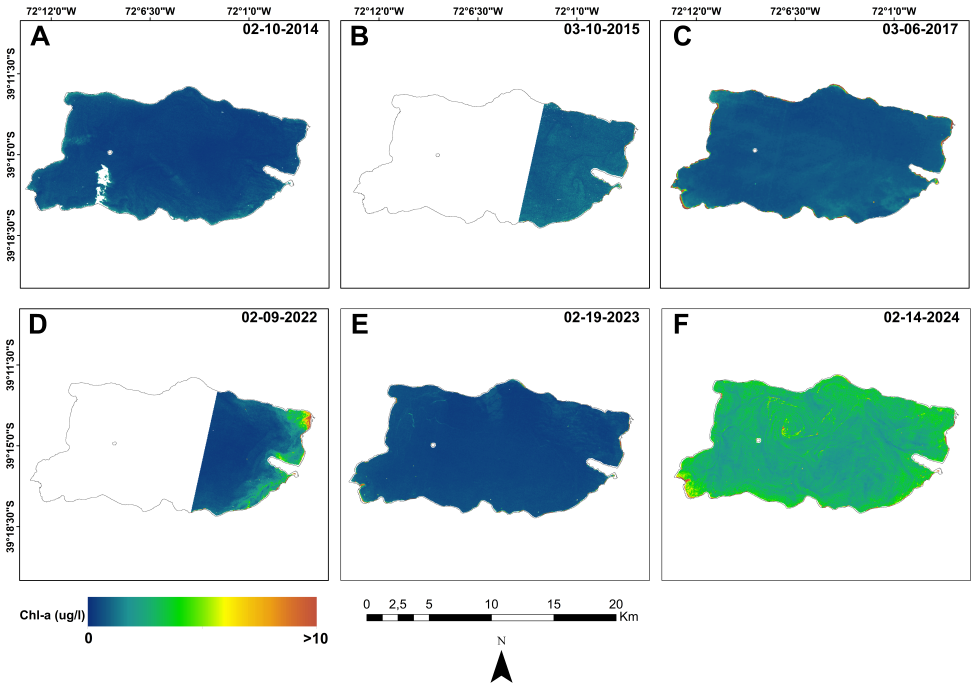

Figure 9: Spatial distribution of Chl-a derived from Landsat-8 and Landsat-9 imagery using the (Red–Blue)/(Red+Blue) index during the summer seasons of 2013–2015 and 2022–2024.

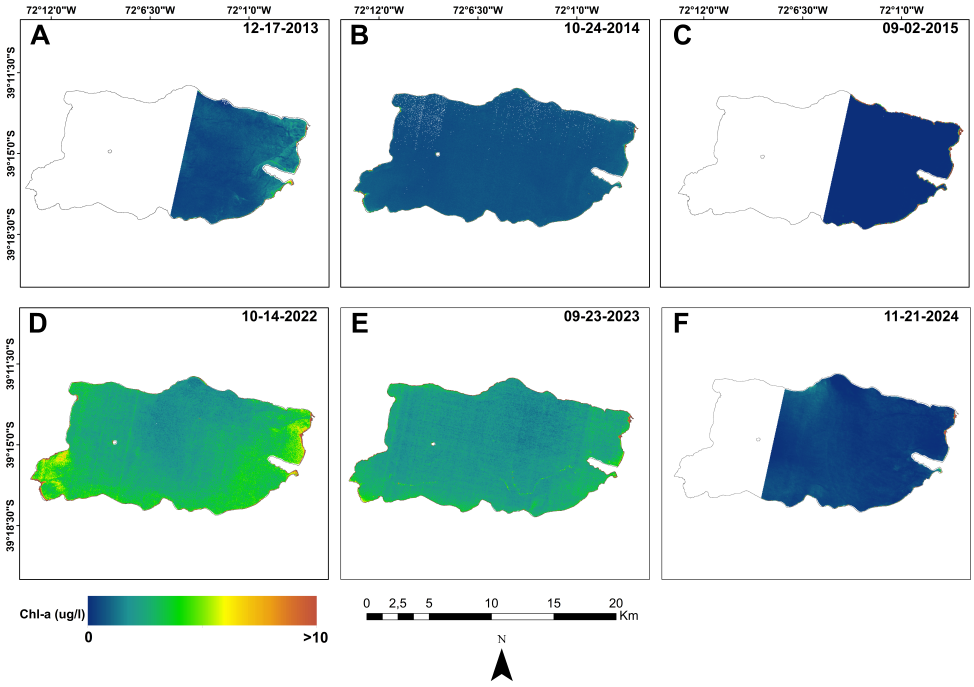

Figure 10: Spatial distribution of Chl-a derived from Landsat-8 and 9 imagery for the (Red-Blue)/(Red+Blue) index for the spring season of the period 2013-2015 and the period 2022-2024.

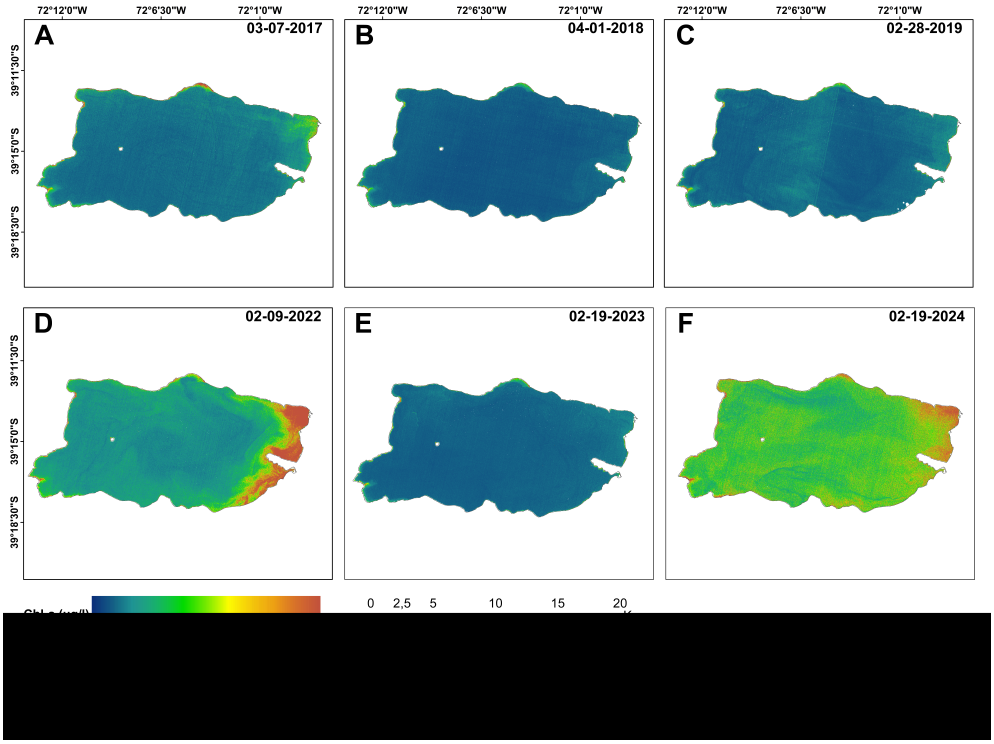

Figure 11: Spatial distribution of Chl-a derived from Sentinel-2A imagery for the Green/Blue index for the summer season for the period 2017-2019 and the period 2022-2024.

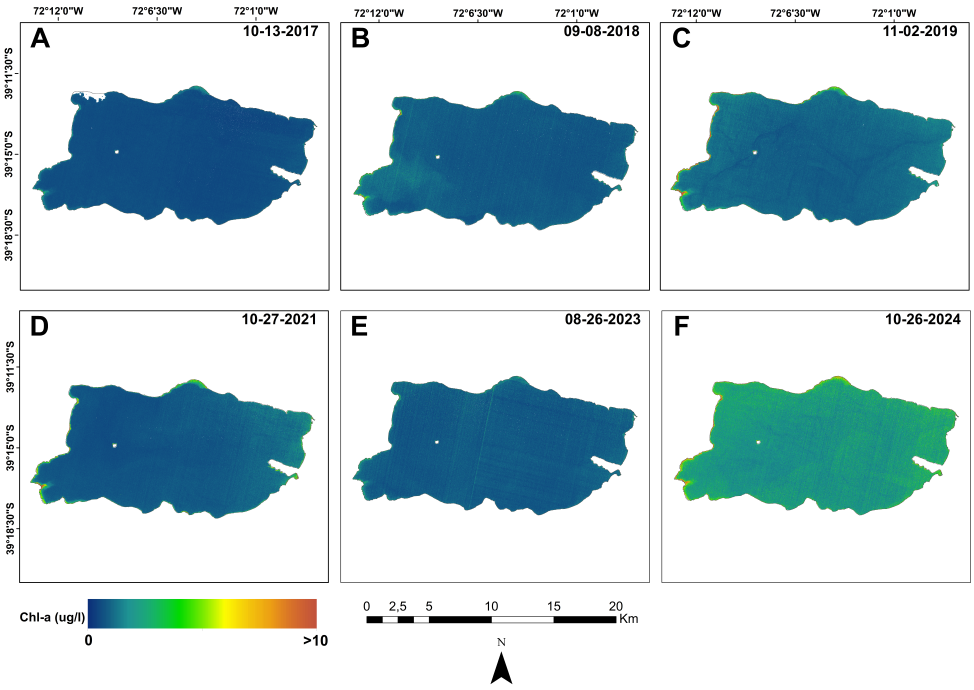

Figure 12: Spatial distribution of Chl-a derived from Sentinel-2A images for the Green/Blue index for the spring season of the period 2017-2019 and the period 2021-2024.

Capítulo 4

Discusión

The results obtained in this study demonstrate the strong potential of multispectral satellite imagery for monitoring Chl-a in oligotrophic and mesotrophic lakes. Both Landsat-8/9 and Sentinel-2A models showed robust relationships between surface reflectance and in-situ Chl-a concentrations. The performance of the exponential models highlights the suitability of empirical approaches for inland waters, particularly in systems characterized by low phytoplankton biomass and high-water transparency, such as Lake Villarrica.

The calibrated satellite-based spectral models revealed significant relationships between reflectance and in-situ Chl-a concentration in Lake Villarrica. In the case of the Landsat-8 and 9 sensors, the selected exponential model achieved a coefficient of determination of $R^2 = 0.79$, with a RMSE of 2.1 µg·L^{-1} and a MAE of 1.2 µg·L^{-1} over a concentration range between 0.1 and 20 µg·L^{-1}. Meanwhile, the model derived from Sentinel-2A, based on a more limited range of in-situ values (0.1–5 µg·L^{-1}), obtained an $R^2 = 0.75$, an RMSE of 0.8 µg·L^{-1} and an MAE of 0.72 µg·L^{-1}. Although the Landsat-8/9 model shows a slightly stronger statistical fit, prediction errors tend to increase at higher concentrations due to the exponential formulation of the model. Similar patterns have been reported in other studies, where exponential relationships perform well at low and moderate concentrations but tend to overestimate Chl-a under high phytoplankton biomass conditions Niroumand-Jadidi et al. (2022); Mansaray et al. (2021); Cantos et al. (2025).

Considering both the concentration range and the number of training samples, the Sentinel-2A model may provide more reliable predictions within its observed range,

as it was trained with a larger dataset (90 samples) and shows lower absolute errors. In contrast, the Landsat-8/9 model covers a broader concentration range, making it more suitable for capturing extreme values and long-term variability, despite being calibrated with fewer observations (60 samples) and showing higher prediction uncertainty at elevated Chl-a levels. These complementary characteristics highlight the advantage of integrating both satellite missions for operational water quality monitoring.

The scatter plots between measured and estimated values indicate a generally good agreement, although deviations increase at the upper end of the distribution. In particular, the Landsat-8/9 model exhibits greater dispersion at higher Chl-a concentrations. This behaviour is consistent with previous observations indicating that exponential models are sensitive to low and moderate concentrations but may overestimate values during bloom events Hafeez et al. (2022); Salls et al. (2024).

The hyperspectral measurements collected with the field spectroradiometer provided valuable insight into the spectral regions most sensitive to variations in Chl-a concentration in Lake Villarrica. The strongest relationships emerged consistently within the visible spectrum, particularly in the blue, green, and red regions, confirming patterns commonly reported for optically complex inland waters. In our analysis, the blue band exhibited the highest explanatory power ($R^2 = 0.88$), followed by the red ($R^2 = 0.82$) and green ($R^2 = 0.80$) bands. These results support the selection of visible-band spectral indices, including blue–green and blue–red combinations, which were identified as the most effective for capturing Chl-a dynamics. Overall, the spectroradiometer data reinforce the suitability of these spectral regions for satellite-based Chl-a retrievals, highlighting their sensitivity to absorption and scattering processes in this eutrophication-prone system.

The strong performance of visible spectral bands observed in this study is consistent with the bio-optical properties of Chl-a, which exhibits absorption features in the blue and red regions and increased reflectance in the green domain. In low biomass environments, these spectral regions remain the most sensitive to phytoplankton variability, while near-infrared and red-edge bands may become less effective due to the dominant absorption by pure water. Similar findings have been reported in oligotrophic lakes in temperate and volcanic regions Meyer et al. (2024); Chen et al. (2024).

The spatial distribution maps (Figure 9 - Figure 12) revealed clear and consistent

patterns of phytoplankton variability. In the Landsat-8/9 time series (2013–2015 and 2022–2024), early years were characterized by low Chl-a concentrations, generally below 2 µg·L^{-1}, reflecting predominantly oligotrophic conditions. In contrast, a gradual upward trend was observed in recent years, particularly during the warm seasons. During the spring of 2022 and 2023, concentrations approached 3–4 µg·L^{-1}, and a localized algal bloom was observed in the eastern sector during the summer of 2022.

The Sentinel-2A retrieval maps (2017–2019 and 2022–2024) provided more detailed spatial information due to the higher spatial resolution of the sensor. A similar temporal trend was observed, with low concentration in earlier years and increased spatial variability in recent periods. In both summer and spring, higher Chl-a concentrations were consistently detected along lake margins, whereas the central pelagic region maintained comparatively lower values.

The temporal comparison between both satellite datasets reveals a consistent pattern of increasing Chl-a in Lake Villarrica, particularly in nearshore zones influenced by tributary inflows and urban areas. These findings suggest that littoral environments are more sensitive to nutrient enrichment and environmental variability. The observed increase in phytoplankton biomass may be linked to a combination of climatic and anthropogenic drivers, including warmer conditions, reduced precipitation, and increasing pressure from urbanization and tourism in the watershed. Similar processes have been reported in other freshwater systems experiencing eutrophication and bloom intensification Zhang et al. (2024); Ho and Michalak (2020); Pérez-Arvizu et al. (2013); Rodríguez-López et al. (2025).

Several limitations should be acknowledged. The trophic state classification relied primarily on Chl-a, and future studies should incorporate complementary indicators such as Secchi depth, Total Phosphorus, and suspended sediment. Temporal discontinuities in the dataset also limited the assessment of long-term interannual variability. In addition, the Sentinel-2A model was calibrated using a restricted range of concentrations, which may reduce its reliability during high-biomass events. Despite these limitations, the integration of field spectroscopy and multisensor satellite imagery demonstrated strong potential for monitoring spatial and temporal variability in phytoplankton biomass. This multisensor approach enhances both temporal and spatial monitoring capacity and supports operational water quality assessment in regions with limited in-situ observations.

Capítulo 5

Conclusión

This study evaluated different spectral-index-based models to estimate Chl-a concentration in Lake Villarrica using Sentinel-2A and Landsat-8/9 satellite imagery atmospherically corrected with ACOLITE. The results demonstrated the strong performance of new band combinations developed in this work, which outperformed commonly used indices such as NDVI and GNDVI. These findings highlight the importance of adapting retrieval algorithms to the optical characteristics of individual lakes rather than relying on generic formulations. This was further supported by field spectroscopy measurements acquired synchronously with in-situ sampling, which validated the spectral relationships observed in the satellite reflectance data.

The complementary performance of Landsat and Sentinel supports multisensor monitoring strategies. These complementary characteristics indicate that Landsat-8/9 provides greater robustness for long-term and high-range variability, whereas Sentinel-2A offers improved sensitivity for detecting subtle spatial and temporal changes in low-biomass conditions. Despite these differences, both models revealed consistent spatial and seasonal patterns of Chl-a distribution, supporting the reliability of the proposed methodology.

The combined use of remote sensing and in-situ observations provides robust evidence of increasing phytoplankton biomass in Lake Villarrica, particularly in nearshore areas exposed to tributary inputs and human activities. This pattern points to a growing vulnerability of littoral zones to nutrient enrichment under ongoing climatic and anthropogenic pressures. Consequently, these results highlight the importance of integrating satellite-based monitoring into operational

management frameworks, enabling early detection of eutrophication hotspots and supporting timely mitigation and watershed management strategies.

Future work should focus on expanding the in-situ database, incorporating additional limnological variables, and increasing temporal coverage. The integration of field spectroscopy and UAV-based multispectral sensors could further improve model accuracy and mitigate limitations related to cloud cover and atmospheric effects. Overall, the proposed approach provides a scalable and cost-effective framework for monitoring lake water quality, with potential applicability to other oligotrophic and mesotrophic volcanic lakes in southern Chile and similar environments worldwide.

Bibliografía

Aguilera, A., Almanza, V., Haakonsson, S., Palacio, H., Benitez Rodas, G. A., Barros, M. U. G., Capelo-Neto, J., Urrutia, R., Aubriot, L., and Bonilla, S. (2023). Cyanobacterial bloom monitoring and assessment in latin america. *Harmful Algae*, 125:102429.

Allam, M. and Allam, Q. (2024). Atmospheric correction algorithms assessment for sentinel-2a imagery over inland waters of china: Case study, qiandao lake. *Earth Systems and Environment*.

Barraza-Moraga, F., Alcayaga, H., Pizarro, A., Félez-Bernal, J., and Urrutia, R. (2022). Estimation of chlorophyll-*a* concentrations in lanalhue lake using sentinel-2 msi satellite images. *Remote Sensing*, 14:5647.

Buma, W. G. and Lee, S.-I. (2020). Evaluation of sentinel-2 and landsat 8 images for estimating chlorophyll-*a* concentrations in lake chad, africa. *Remote Sensing*, 12:2437.

Campero, M., Balseiro, E., Fernández, C. E., Modenutti, B., Prado, P. E., Rivera-Rondon, C. A., Carvajal-Vallejos, F. M., Herrera-Martínez, Y., López-París, M. D., Aranguren-Riaño, N., et al. (2024). Andean lakes: Endangered by natural and anthropogenic threats. *Inland Waters*, pages 1–72.

Cantos, V. F. F., Rodríguez, P. X. L., Izurieta, J. E. A., Santillán, C. A. J., Ruiz-Verdú, A., Verrelst, J., Goethals, P. L. M., and Delegido, J. (2025). Spatiotemporal analysis of water quality conditions in high-andean lakes based on satellite indicators using sentinel-2 and landsat-8/9 images. *Water*, 17(21):3145.

Carlson, R. E. (1977). A trophic state index for lakes. *Limnology and Oceanography*, 22:361–369.

Chen, F., Li, S., and Song, K. (2024). Remote sensing of lake chlorophyll-a in qinghai-tibet plateau responding to climate factors: Implications for oligotrophic lakes. *Ecological Indicators*, 159:111674.

Cillero Castro, C., Domínguez Gómez, J. A., Delgado Martín, J., Hinojo Sánchez, B. A., Cereijo Arango, J. L., Cheda Tuya, F. A., and Díaz-Varela, R. (2020). An uav and satellite multispectral data approach to monitor water quality in small reservoirs. *Remote Sensing*, 12:1514.

Cáceres-Merino, J., Cuartero, A., and Torrecilla-Piñero, J. A. (2024). Finding optimal window size: The influence of methodology on remote-sensing based chlorophyll-*a* prediction in small reservoirs. Manuscript in press.

Dagnino S., J. (2014). Correlación. *Revista Chilena de Anestesia*, 43.

Dirección General de Aguas (DGA) (2014). Evaluación de la condición trófica: Red de control de lagos. Technical report, Ministerio de Obras Públicas, Gobierno de Chile, Santiago, Chile. Informe técnico.

Dirección General de Aguas (DGA) (2016). *Atlas del Agua Chile 2016*. Ministerio de Obras Públicas, Gobierno de Chile, Santiago, Chile. Primera edición.

Dirección General de Aguas (DGA) (2017). Reporte de la red de control de lagos de la dirección general de aguas. año 2017. Technical report, Ministerio de Obras Públicas, Dirección General de Aguas, Santiago, Chile. Departamento de Conservación y Protección de Recursos Hídricos.

Dirección General de Aguas (DGA) (2018). Análisis de la relación entre la concentración de clorofila *a* y la transparencia de los lagos monitoreados por la red de calidad de la dga, y elaboración de un ranking de lagos basado en el estado trófico otorgado por estos parámetros. Technical report, Ministerio de Obras Públicas, Gobierno de Chile, Santiago, Chile. Informe técnico.

Dokulil, M. T. (2014). Environmental impacts of tourism on lakes. In Ansari, A. A. and Gill, S. S., editors, *Eutrophication: Causes, Consequences and Control*, pages 81–88. Springer Netherlands, Dordrecht.

European Space Agency (2023). Sentinel-2 msi spectral response functions (s2-srf). Technical report, European Space Agency. Available online.

European Space Agency (ESA) (2025). Copernicus browser. https://browser.dataspace.copernicus.eu/?zoom=5&lat=50.16282&lng=20.78613&themeId=DEFAULT-THEME&demSource3D=%22MAPZEN%22&cloudCoverage=30&dateMode=SINGLE. Accessed on 12 May 2025.

Fernández, B. and Gironás, J. (2021). *Water Resources of Chile*. Springer.

Frampton, W. J., Dash, J., Watmough, G., and Milton, E. J. (2013). Evaluating the capabilities of sentinel-2 for quantitative estimation of biophysical variables in vegetation. *ISPRS Journal of Photogrammetry and Remote Sensing*, 82:83–92.

German, A., Nemiña, F., Scavuzzo, C. M., and Ferral, A. (2024). Evaluation of acolite software for atmospheric and glint correction in sentinel-2 imagery: Implications for algae bloom monitoring in eutrophic reservoirs. In *Proceedings of the IGARSS 2024 - 2024 IEEE International Geoscience and Remote Sensing Symposium*, pages 5015–5018, Athens, Greece. IEEE.

Gholizadeh, M., Melesse, A., and Reddi, L. (2016). A comprehensive review on water quality parameters estimation using remote sensing techniques. *Sensors*, 16:1298.

Goyens, C., Lavigne, H., Dille, A., and Vervaeren, H. (2022). Using hyperspectral remote sensing to monitor water quality in drinking water reservoirs. *Remote Sensing*, 14(21):5607.

Hafeez, S., Wong, M. S., Abbas, S., and Asim, M. (2022). Evaluating landsat-8 and sentinel-2 data consistency for high spatiotemporal inland water quality monitoring. *Remote Sensing*, 14(13):3155.

Han, Q. and Niu, Z. (2020). Construction of the long-term global surface water extent dataset based on water-ndvi spatio-temporal parameter set. *Remote Sensing*, 12:2675.

Heino, J., Alahuhta, J., Bini, L. M., Cai, Y., Heiskanen, A.-S., Hellsten, S., Kortelainen, P., Kotamäki, N., Tolonen, K. T., Vihervaara, P., et al. (2021). Lakes in the era of global change: Moving beyond single-lake thinking in maintaining biodiversity and ecosystem services. *Biological Reviews*, 96:89–106.

Herrera, J. S. B. (2021). Diagnóstico de la condición trófica del lago villarrica utilizando imágenes satelitales. Tesis de magíster, Universidad no especificada, Chile. Trabajo académico no publicado.

Ho, J. C. and Michalak, A. M. (2020). Exploring temperature and precipitation impacts on harmful algal blooms across continental u.s. lakes. *Limnology and Oceanography*, 65(5):992–1009.

Hyndman, R. J. and Athanasopoulos, G. (2018). *Forecasting: Principles and Practice*. OTexts, Lexington, KY, 2nd edition. Online open-access textbook.

Instituto de Investigaciones Agropecuarias (INIA) (2025). Agrometeorología | inia. https://agrometeorologia.cl/. Accessed on 12 May 2025.

Jang, W., Kim, J., Kim, J.-H., Shin, J.-K., Chon, K., Kang, E.-T., Park, Y., and Kim, S. (2024). Evaluation of sentinel-2 based chlorophyll-a estimation in a small-scale reservoir: Assessing accuracy and availability. *Remote Sensing*, 16:315.

Karimi, B., Hashemi, S. H., and Aghighi, H. (2024). Application of landsat-8 and sentinel-2 for retrieval of chlorophyll-a in a shallow freshwater lake. *Advances in Space Research*, 74:117–129.

Ladera Sur (2024). Sigue el problema: Nuevo bloom de algas en lago villarrica alerta a la comunidad. https://laderasur.com/articulo/sigue-el-problema-nuevo-bloom-de-algas-en-lago-villarrica-alerta-a-la-comunidad/. Accessed on 19 May 2024.

Li, S., Kutser, T., Song, K., Liu, G., and Li, Y. (2023). Lake turbidity mapping using an owts-bp based framework and sentinel-2 imagery. *Remote Sensing*, 15:2489.

Lin, Y., Gao, J., Tu, Y., Zhang, Y., and Gao, J. (2024). Estimating low

concentration heavy metals in water through hyperspectral analysis and genetic algorithm-partial least squares regression. *Science of The Total Environment*, 916:170225.

Mabit, R., Araújo, C. A. S., Singh, R. K., and Bélanger, S. (2022). Empirical remote sensing algorithms to retrieve SPM and CDOM in québec coastal waters. *Frontiers in Remote Sensing*, 3:834908.

Mamun, M., Hasan, M., and An, K.-G. (2024). Advancing reservoirs water quality parameters estimation using sentinel-2 and landsat-8 satellite data with machine learning approaches. *Ecological Informatics*, 81:102608.

Mansaray, A. S., Dzialowski, A. R., Martin, M. E., Wagner, K. L., Gholizadeh, H., and Stoodley, S. H. (2021). Comparing planetscope to landsat-8 and sentinel-2 for sensing water quality in reservoirs in agricultural watersheds. *Remote Sensing*, 13(9):1847.

Mansourmoghaddam, M., Ghafarian Malamiri, H. R., Rousta, I., Olafsson, H., and Zhang, H. (2022). Assessment of palm jumeirah island's construction effects on the surrounding water quality and surface temperatures during 2001–2020. *Water*, 14:634.

Meyer, M. F., Topp, S. N., King, T. V., Ladwig, R., Pilla, R. M., Dugan, H. A., and Zwart, J. A. (2024). National-scale remotely sensed lake trophic state from 1984 through 2020. *Scientific Data*, 11(1):77.

Milton, E. J. (1987). Principles of field spectroscopy. *International Journal of Remote Sensing*, 8:1807–1827.

Ministerio del Medio Ambiente (MMA) (2017). Decreto supremo n.º 43: Declara zona saturada por clorofila *a*, transparencia y fósforo disuelto a la cuenca del lago villarrica. Technical report, Ministerio del Medio Ambiente, Gobierno de Chile. Publicación oficial en el Diario Oficial de la República de Chile.

Ministerio del Medio Ambiente (MMA) (2020). Anteproyecto del plan de descontaminación por clorofila *a*, transparencia y fósforo disuelto para la cuenca del lago villarrica. Technical report, Ministerio del Medio Ambiente, Gobierno de Chile. Disponible en línea.

Mishra, S. and Mishra, D. R. (2012). Normalized difference chlorophyll index: A novel model for remote estimation of chlorophyll-a concentration in turbid productive waters. *Remote Sensing of Environment*, 117:394–406.

Mobley, C. D. (1999). Estimation of the remote-sensing reflectance from above-surface measurements. *Applied Optics*, 38(36):7442–7455.

Muramatsu, K. (2019). Use of chlorophyll index-green and the red-edge chlorophyll index to derive an algorithm for estimating gross primary production capacity. In *Proceedings of SPIE*, volume 11149, page 1114906, Bellingham, WA, USA. SPIE.

Ngamile, S., Madonsela, S., and Kganyago, M. (2025). Trends in remote sensing of water quality parameters in inland water bodies: A systematic review. *Frontiers in Environmental Science*, 13:1549301.

Nguyen, V. S., Loisel, H., Vantrepotte, V., Mériaux, X., and Tran, D. L. (2024). An empirical algorithm for estimating the absorption of colored dissolved organic matter from sentinel-2 (msi) and landsat-8 (oli) observations of coastal waters. *Remote Sensing*, 16:4061.

Nimptsch, J., Woelfl, S., Osorio, S., Valenzuela, J., Moreira, C., Ramos, V., Castelo-Branco, R., Leão, P. N., and Vasconcelos, V. (2016). First record of toxins associated with cyanobacterial blooms in oligotrophic north patagonian lakes of chile — a genomic approach. *International Review of Hydrobiology*, 101:57–68.

Niroumand-Jadidi, M., Bovolo, F., Bresciani, M., Gege, P., and Giardino, C. (2022). Water quality retrieval from landsat-9 (oli-2) imagery and comparison to sentinel-2. *Remote Sensing*, 14(18):4596.

Niu, X., Chen, B., Sun, W., Feng, T., Yang, X., Liu, Y., Liu, W., and Fu, B. (2024). Estimation of coastal wetland vegetation aboveground biomass by integrating uav and satellite remote sensing data. *Remote Sensing*, 16:2760.

Ogashawara, I., Kiel, C., Jechow, A., Kohnert, K., Ruhtz, T., Grossart, H.-P., Hölker, F., Nejstgaard, J. C., Berger, S. A., and Wollrab, S. (2021). The use of sentinel-2 for chlorophyll-*a* spatial dynamics assessment: A comparative study on different lakes in northern germany. *Remote Sensing*, 13:1542.

Pahlevan, N., Mangin, A., Balasubramanian, S. V., Smith, B., Alikas, K., Arai, K., Barbosa, C., Bélanger, S., Binding, C., Bresciani, M., et al. (2021). Acix-aqua: A global assessment of atmospheric correction methods for landsat-8 and sentinel-2 over lakes, rivers, and coastal waters. *Remote Sensing of Environment*, 258:112366.

Pan, X., Yuan, J., Yang, Z., Tansey, K., Xie, W., Song, H., Wu, Y., and Yang, Y. (2024). Spatio-temporal variation of cyanobacteria blooms in taihu lake using multiple remote sensing indices and machine learning. *Remote Sensing*, 16:889.

Pérez-Arvizu, E. M., Aragón-Noriega, E. A., and Espinosa-Carreón, T. L. (2013). Variabilidad estacional de la clorofila a y su respuesta a condiciones El Niño y La Niña en el norte del golfo de california. *Revista de Biología Marina y Oceanografía*, 48(1):131–141.

Richardson, D., Melles, S., Pilla, R., Hetherington, A., Knoll, L., Williamson, C., Kraemer, B., Jackson, J., Long, E., Moore, K., et al. (2017). Transparency, geomorphology and mixing regime explain variability in trends in lake temperature and stratification across northeastern north america (1975–2014). *Water*, 9:442.

Rodríguez-López, L., Usta, D. F. B., Durán-Llacer, I., Álvarez, L. B., Bourrel,

L., Frappart, F., and Urrutia, R. (2025). Advanced phycocyanin detection in a south american lake using landsat imagery and remote sensing. *Frontiers in Remote Sensing*, 6:1633522.

Rodríguez-López, L., Alvarez, D., Bustos Usta, D., Duran-Llacer, I., Bravo Alvarez, L., Fagel, N., Bourrel, L., Frappart, F., and Urrutia, R. (2024). Chlorophyll-*a* detection algorithms at different depths using in situ, meteorological, and remote sensing data in a chilean lake. *Remote Sensing*, 16:647.

Rodríguez-López, L., Duran-Llacer, I., Bravo Alvarez, L., Lami, A., and Urrutia, R. (2023a). Recovery of water quality and detection of algal blooms in lake villarrica through landsat satellite images and monitoring data. *Remote Sensing*, 15:1929.

Rodríguez-López, L., Usta, D. B., Duran-Llacer, I., Alvarez, L. B., Yépez, S., Bourrel, L., Frappart, F., and Urrutia, R. (2023b). Estimation of water quality parameters through a combination of deep learning and remote sensing techniques in a lake in southern chile. *Remote Sensing*, 15:4157.

Salls, W., Schaeffer, B., Pahlevan, N., Coffer, M., Seegers, B., Werdell, P., Ferriby, H., Stumpf, R., Binding, C., and Keith, D. (2024). Expanding the application of sentinel-2 chlorophyll monitoring across united states lakes. *Remote Sensing*, 16(11):1977.

Simón, J. W. and Ceballos Sáez, C. (2023). Análisis del proceso de gobernanza colaborativa para abordar un problema socioambiental en un contexto conflictivo. *Estudios Sociales y Territoriales (EST)*, pages 629–660.

Sivakumar, V., Kannan, V., Uppara, R. B., Sasivarman, B., Srinivasan, N., and Velusamy, P. (2024). Spatiotemporal variation of water quality in the context of suspended particulate matter in laguna mar chiquita lake, argentina using acolite. *Desalination and Water Treatment*, 320:100684.

Talavera, L., Domínguez-Gómez, J. A., Navarro, N., and Rodríguez-Santalla, I. (2024). Analysing spatiotemporal variability of chlorophyll-*a* concentration and water surface temperature in coastal lagoons of the ebro delta (nw mediterranean sea, spain). *Journal of Marine Science and Engineering (JMSE)*, 12:941.

United States Geological Survey (USGS) (2025). Earthexplorer. https://earthexplorer.usgs.gov/. Accessed on 12 May 2025.

U.S. Geological Survey (2021). Spectral response of the operational land imager (oli). Technical report, U.S. Geological Survey, Reston, VA, USA. Technical Document.

Vanhellemont, Q., Dogliotti, A., Doxaran, D., Goyens, C., Ruddick, K., and Vansteenwegen, D. (2024). Remote sensing of turbid coastal and estuarine waters with viirs i (375 m) and m (750 m) bands. *International Journal of Remote Sensing*, 45:9162–9191.

Vanhellemont, Q. and Ruddick, K. (2018). Atmospheric correction of metre-scale optical satellite data for inland and coastal water applications. *Remote Sensing of Environment*, 216:586–597.

Vanhellemont, Q. and Ruddick, K. (2021). Atmospheric correction of sentinel-3/olci data for mapping of suspended particulate matter and chlorophyll-*a* concentration in belgian turbid coastal waters. *Remote Sensing of Environment*, 256:112284.

Vaughn, N. R., König, M., Hondula, K. L., Harrison, D. E., and Asner, G. P. (2024). Rapid water quality mapping from imaging spectroscopy with a superpixel approach to bio-optical inversion. *Remote Sensing*, 16(23):4344.

Wang, D., Tang, B.-H., and Li, Z.-L. (2024a). Evaluation of five atmospheric correction algorithms for multispectral remote sensing data over plateau lake. *Ecological Informatics*, 82:102666.

Wang, Z., Ding, J., Tan, J., Liu, J., Zhang, T., Cai, W., and Meng, S. (2024b). Uav hyperspectral analysis of secondary salinization in arid oasis cotton fields: effects of fod feature selection and soa-rf. *Frontiers in Plant Science*, 15:1358965.

Xing, D., Sun, P., Wang, Y., Jiang, M., Miao, S., Liu, W., Huang, H., and Lin, E. (2024). Non-destructive estimation of needle leaf chlorophyll and water contents in chinese fir seedlings based on hyperspectral reflectance spectra. *Frontiers of Research in Environment and Sustainability*, 4:0021.

Xu, H., Ren, M., and Lin, M. (2024). Cross-comparison of landsat-8 and landsat-9 data: A three-level approach based on underfly images. *GIScience & Remote Sensing*, 61:2318071.

Yepez, S., Laraque, A., Martinez, J.-M., De Sa, J., Carrera, J. M., Castellanos, B., Gallay, M., and Lopez, J. L. (2017). Retrieval of suspended sediment concentrations using Landsat-8 OLI satellite images in the orinoco river (venezuela). *Comptes Rendus. Géoscience*, 350:20–30.

Yépez, S., Velásquez, G., Torres, D., Saavedra-Passache, R., Pincheira, M., Cid, H., Rodríguez-López, L., Contreras, A., Frappart, F., Cristóbal, J., Pons, X., Flores, N., and Bourrel, L. (2024). Spatiotemporal variations in biophysical water quality parameters: An integrated in situ and remote sensing analysis of an urban lake in chile. *Remote Sensing*, 16(2):427.

Yépez, S., Velásquez, G., Torres, D., Saavedra-Passache, R., Pincheira, M., Cid, H., Rodríguez-López, L., Contreras, A., Frappart, F., Cristóbal, J., et al. (2024). Spatiotemporal variations in biophysical water quality parameters: An integrated in situ and remote sensing analysis of an urban lake in chile. *Remote Sensing*, 16:427.

Zadereev, E., Lipka, O., Karimov, B., Krylenko, M., Elias, V., Pinto, I. S., Alizade, V., Anker, Y., Feest, A., Kuznetsova, D., et al. (2020). Overview of past, current,

and future ecosystem and biodiversity trends of inland saline lakes of europe and central asia. *Inland Waters*, 10:438–452.

Zhang, Y., Shen, J., He, L., Feng, J., Chi, L., and Wang, X. (2024). Challenge to lake ecosystems: Changes in thermal structure triggered by climate change. *Water*, 16:888.

Zhao, D., Huang, J., Li, Z., Yu, G., and Shen, H. (2024). Dynamic monitoring and analysis of chlorophyll-*a* concentrations in global lakes using sentinel-2 images in google earth engine. *Science of The Total Environment*, 912:169152.

Zumelzu, M. S. (2021). Migración por estilos de vida y tensiones socioterritoriales: El caso de villarrica–pucón en un horizonte postpandemia. Tesis de magíster en asentamientos humanos y medio ambiente, Instituto de Estudios Urbanos y Territoriales, Facultad de Arquitectura, Diseño y Estudios Urbanos, Universidad Católica de Chile, Santiago, Chile.

A1. Appendix A

Table A1. Information from the DGA monitoring stations in force in Lake Villarrica.

Station	Id	Latitude	Longitude
Litoral Villarrica	V1	39°16'55.67"S	72°12'33.44"W
Pelagial Villarrica	V2	39°16'22.13"S	72°11'1.56"W
Litoral Norte	V3	39°12'37.30"S	72°8'30.02"W
Sector Centro	V4	39°15'32.05"S	72°5'27.77"W
Litoral Sur	V5	39°17'26.04"S	72°5'31.29"W
Litoral Pucón	V6	39°15'57.17"S	71°58'55.38"W
La Poza	V7	39°16'37.64"S	71°59'9.57"W

A2. Appendix B

Table B1. Summary of satellite imagery used from Landsat and Sentinel missions.

Satellite	Date	N° Images
Landsat-8 and 9	2013–2024	17
Sentinel-2A	2016–2024	14
Sentinel-2B	2020–2024	11
Sentinel-2A&B$^{(*)}$	2016–2024	18

$^{(*)}$ Combined acquisitions from both Sentinel-2A and 2B satellites.

Table B2. Information on Landsat-8 and Landsat-9 imagery.

N	L8 & L9 Image ID	Year	*In-situ Data*	Imagen Date	Days differences
1	LC08_L1TP_233087_20131201_20200912_02_T1	2013	15 Nov.	1 Dec.	±15
2	LC08_L1TP_233087_20140125_20200912_02_T1	2014	3 Feb.	25 Jan.	±8
3	LC08_L1TP_233087_20141024_20200910_02_T1	2014	7 Oct.	24 Oct.	±17
4	LC08_L1TP_233087_20150128_20200909_02_T1	2015	27 Jan.	28 Jan.	±1
5	LC08_L1TP_233087_20151011_20200908_02_T1	2015	19 Oct.	11 Oct.	±8
6	LC08_L1TP_233087_20161013_20200905_02_T1	2016	18 Oct.	13 Oct.	±5
7	LC08_L1TP_233087_20170306_20200905_02_T1	2017	1 Mar.	6 Mar.	±5
8	LC08_L1TP_233087_20200211_20200823_02_T1	2020	29 Jan.	11 Feb.	±13
9	LC08_L1TP_233087_20200314_20200822_02_T1	2020	27 Feb.	14 Mar.	±15
10	LC08_L1TP_232087_20211105_20211116_02_T1	2021	8 Nov.	5 Nov.	±3
11	LC08_L1TP_232087_20220209_20220222_02_T1	2022	7 Feb.	9 Feb.	±2
12	LC09_L1TP_232087_20220305_20230425_02_T1	2022	2 Mar.	5 Mar.	±3
13	LC08_L1TP_233087_20230203_20230209_02_T1	2023	25 Jan.	3 Feb.	±9
14	LC08_L1TP_233087_20230228_20230315_02_T1	2023	1 Mar.	28 Feb.	±1
15	LC09_L1TP_233087_20231025_20231025_02_T1	2023	25 Oct.	25 Oct.	±0
16	LC08_L1TP_233087_20231213_20240102_02_T1	2023	10 Dec.	13 Dec.	±3
17	LC08_L1TP_233087_20240325_20240403_02_T1	2024	10 Mar.	25 Mar.	±15

Table B3. Information on Sentinel-2A imagery.

N	S2-A Image ID	Year	*In-situ Data*	Imagen Date	Days differences
1	S2A_MSIL1C_20160305T143722_N0201_R096_T18HYB_20160305T145155	2016	2 Mar.	5 Mar.	±3
2	S2A_MSIL1C_20170307T142851_N0500_R053_T18HYB_20231024T123700.SAFE	2017	1 Mar.	7 Mar.	±6
3	S2A_MSIL1C_20200124T143651_N0208_R096_T19HBS_20200124T175925	2020	28 Jan.	24 Jan.	±4
4	S2A_MSIL1C_20200301T142731_N0500_R053_T19HBS_20230626T093402.SAFE	2020	27 Feb.	1 Mar.	±2
5	S2A_MSIL1C_20201020T143731_N0209_R096_T19HBS_20201020T181238	2020	20 Oct.	20 Oct.	±0
6	S2A_MSIL1C_20201106T142741_N0500_R053_T19HBS_20230620T120239	2020	10 Nov.	6 Nov.	±4
7	S2A_MSIL1C_20201126T142731_N0500_R053_T19HBS_20230406T061335	2020	26 Nov.	26 Nov.	±0
8	S2A_MSIL1C_20211121T142731_N0500_R053_T18HYB_20230101T112123	2021	8 Nov.	21 Nov.	±13
9	S2A_MSIL1C_20230227T143721_N0509_R096_T18HYB_20230227T193828	2023	1 Mar.	27 Feb.	±2
10	S2A_MSIL1C_20231012T142711_N0509_R053_T18HYB_20231012T191303	2023	4 Oct.	12 Oct.	±8
11	S2A_MSIL1C_20231025T143731_N0509_R096_T19HBS_20231025T193949	2023	25 Oct.	25 Oct.	±0
12	S2A_MSIL1C_20231124T143741_N0509_R096_T19HBS_20231124T180437	2023	9 Dec.	24 Nov.	±15
13	S2A_MSIL1C_20240310T142711_N0510_R053_T19HBS_20240310T191925	2024	10 Mar.	10 Mar.	±0
14	S2A_MSIL1C_20241026T142711_N0511_R053_T19HBS_20241026T174914	2024	29 Oct.	26 Oct.	±3

A3. Appendix C

Table C1. Comparative evaluation of exponential and linear models for estimating chlorophyll-a from spectral indices derived from Landsat-8/9 and Sentinel-2A, showing their performance using R^2, RMSE, and MAE

Metrics	**Landsat-8/9 (Exponential model)**	**Landsat-8/9 (Linear model)**	**Sentinel-2A (Exponential model)**	**Sentinel-2A (Linear model)**
Bands used	Red, Blue	Red, Blue	Green, Blue	Green, Blue
General equation	$Y = 56{,}8e^{-7{,}4x}$	$Y = -19{,}01x + 11{,}89$	$Y = 0{,}06e^{3{,}05x}$	$Y = 5{,}4x - 4$
Independent variable	$\frac{Blue - Red}{Blue + Red}$	$\frac{Blue - Red}{Blue + Red}$	$\frac{Green}{Blue}$	$\frac{Green}{Blue}$
Coefficient of determination (R^2)	0.79	0.53	0.75	0.59
RMSE	2.1	3.14	0.88	1.1
MAE	1.2	1.69	0.72	0.8